

Superior high-temperature strength of a carbide-reinforced high-entropy alloy with ultrafine eutectoid structure

Xiao Wang^{a,c}, Guoqiang Luo^{a,c}, Qinjin Wei^{a,b,c,*}, Yi Sun^{a,b,*}, Wei Huang^a, Jian Peng^a, Jian Zhang^a, Qiang Shen^a

^a State Key Lab of Advanced Technology for Materials Synthesis and Processing, Wuhan University of Technology, Wuhan, 430070, PR China

^b Hubei Longzhong Laboratory, Xiangyang 441000, Hubei, PR China

^c School of Materials Science and Engineering, Wuhan University of Technology, Wuhan, 430070, PR China

ARTICLE INFO

Keywords:

High-entropy alloy
Eutectoid structure
High-temperature strength
Microstructure stability

ABSTRACT

Refractory alloys with high-temperature softening resistance are crucial for extreme high-temperature components in aerospace and weapon equipment. Traditional alloys and single-phase refractory high-entropy alloys suffer from unstable microstructures and loss of strength at high temperatures. Here we report a strategy to obtain a superior strong high-entropy alloy by introducing carbides to form micro-nano scale eutectic and eutectoid structures. These metal-carbide interfaces remain stable under high-temperature deformation and exhibit strong dislocation blocking effects. The ultrafine eutectoid structure provides a primary strengthening effect due to its numerous enhanced phase interfaces. The resulting alloy achieves a high temperature yield strength of 1.17 GPa at 1473 K and 0.92 GPa at 1673 K. This work provides valuable insights for optimizing the high-temperature performance and microstructure design of high-temperature composites to further extend their potential applications in high-temperature areas.

Refractory alloys with high-temperature softening resistance are in high demand for extreme high-temperature components in aerospace and weapon equipment fields, such as combustion chambers and nozzles with a working temperature higher than 1473 K [1–13]. Traditional nickel-based alloys typically operate within a temperature range from 873 to 1473 K, further increase in temperature results in a rapid decline in strength due to high-temperature softening and grain boundary coarsening [14]. In contrast, refractory high-entropy alloys (HEAs) have exceptional high-temperature strength due to their high mixing entropy [15,16]. For example, MoNbTaW and MoNbTaWV alloys have a high engineering compressive yield strength of above 400 MPa and an ultimate strength of 470 MPa at 1873 K [17–21]. However, these refractory HEAs lose strength above 1473 K due to rapid grain coarsening.

Eutectic HEAs with two phases distributed alternately have been demonstrated to have high-temperature structural stability. The layered hard second phases improve the structural stability and enhance the alloys by hindering grain coarsening and grain boundary slip [22–30]. Representative of these is the AlCoCrFeNi_{2.1} eutectic HEA, with a fine eutectic microstructure composed of soft FCC and hard BCC phases, exhibiting improved stability and high-temperature strength [28].

However, these eutectic HEAs also show limited high-temperature softening resistance owing to their relatively low melting points of approximately 1673 K.

To overcome the melting point limitation, refractory eutectic HEAs are developed, wherein eutectic carbides are introduced into refractory HEAs to enhance their strength, as seen in alloys such as C_xHf_{0.25}NbTaW_{0.5} [30], NbTaW_{0.5}(Mo₂C)_x [31], and Re_{0.5}MoNbW(TaC)_x [32]. These alloys are composed of BCC HEA and hard carbide phases, both with high melting points. The eutectic carbides were formed in-situ with the BCC HEAs during the solidification process; thus, the phase interfaces exhibit relatively low interfacial energy and high thermal stability, resulting in high-temperature strength. Unfortunately, recrystallization occurred in the 1473 K-deformed C_xHf_{0.25}NbTaW_{0.5} alloy [30], whereas the maximum research temperature for the Re_{0.5}MoNbW(TaC)_x alloy is only up to 1473 K, and adding Re is too expensive.

Inspired by the refractory eutectic-carbide-reinforced HEAs, we have designed novel MoNbW(TaC)_x alloys, in which ultrafine eutectoid structures are promoted to form [26,27,29–32]. The fine layer eutectic structure has been suggested to exhibit improved strength, indicating a

* Corresponding authors.

E-mail addresses: weiqq@whut.edu.cn (Q. Wei), sunyiwhtu@163.com (Y. Sun).

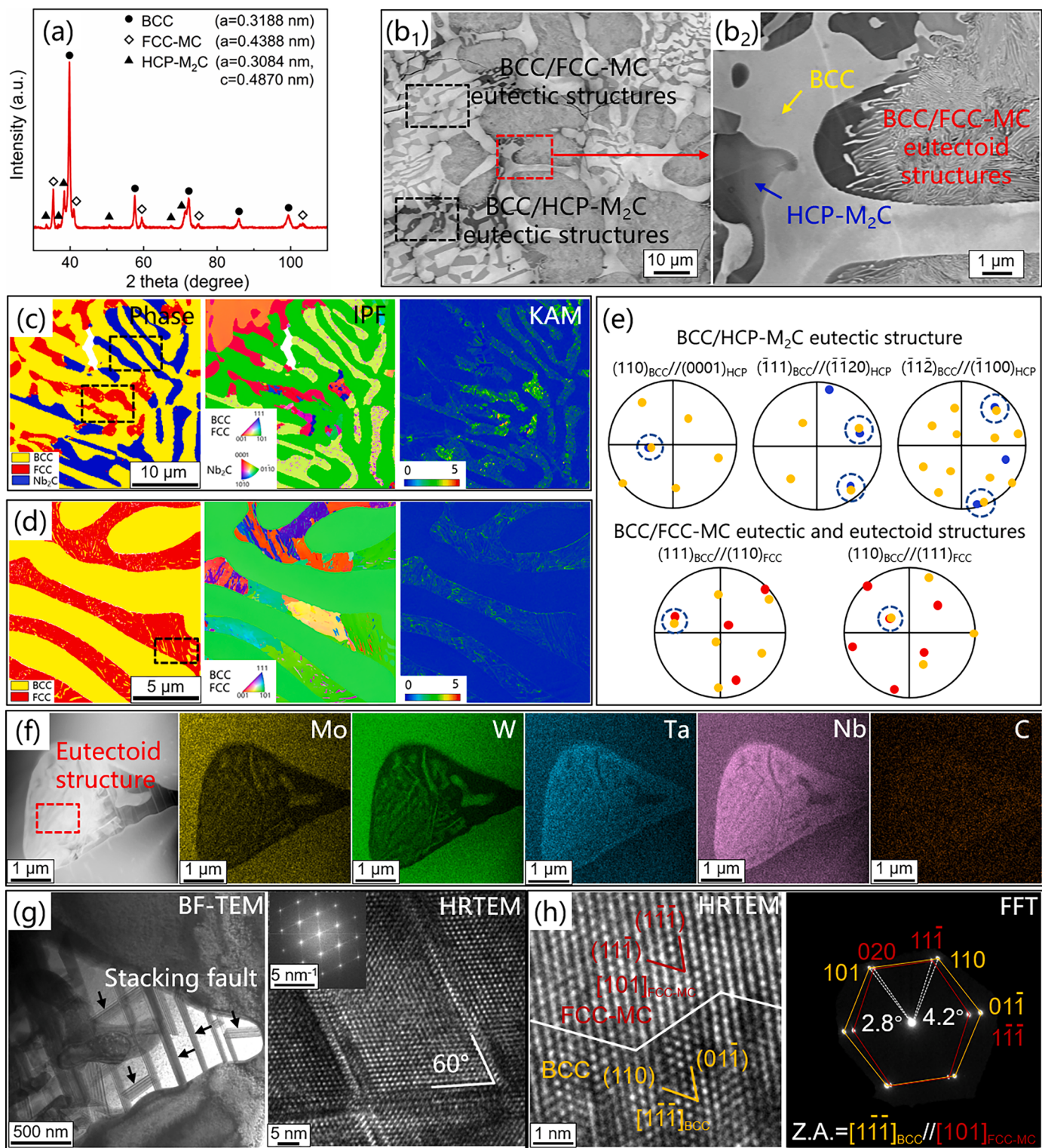


Fig. 1. Microstructures of the as-cast MoNbWTaC HEA. (a-b) XRD pattern and SEM-BSE images. (c-d) EBSD phase map, inverse pole figure (IPF), and KAM maps of the eutectic and eutectoid structures. (e) Orientation relationship maps of the BCC and carbide phases. The PF map is extracted from eutectic regions marked by black rectangles in IPF, the blue circles depicts coincident poles. (f) HAADF-STEM image and the corresponding EDX mapping. (g) Bright-field TEM and high-resolution TEM images show stacking fault in the FCC-MC carbide. (h) High-resolution TEM image and the corresponding FFT pattern show the BCC/FCC-MC interfacial structure. (For interpretation of the references to colour in this figure legend, the reader is referred to the web version of this article.)

better reinforcement effect from the smaller eutectoid structures with decreased interlayer spacing. Therefore, in this study, we demonstrate that the MoNbWTaC HEA achieve exceptional thermal stability and high-temperature strength. The results show that MoNbWTaC HEA exhibits superior yield strengths of 1.17 GPa at 1473 K and 0.92 GPa at

1673 K, along with high compressive strengths of 2.35 GPa at 1473 K and 1.53 GPa at 1673 K. The high-temperature strengthening mechanisms from both the stable metal-carbide semi-coherent interfaces and ultrafine eutectoid structure are systematically studied.

Mo, Nb, W, and TaC powders with a high purity above 99.9% and a

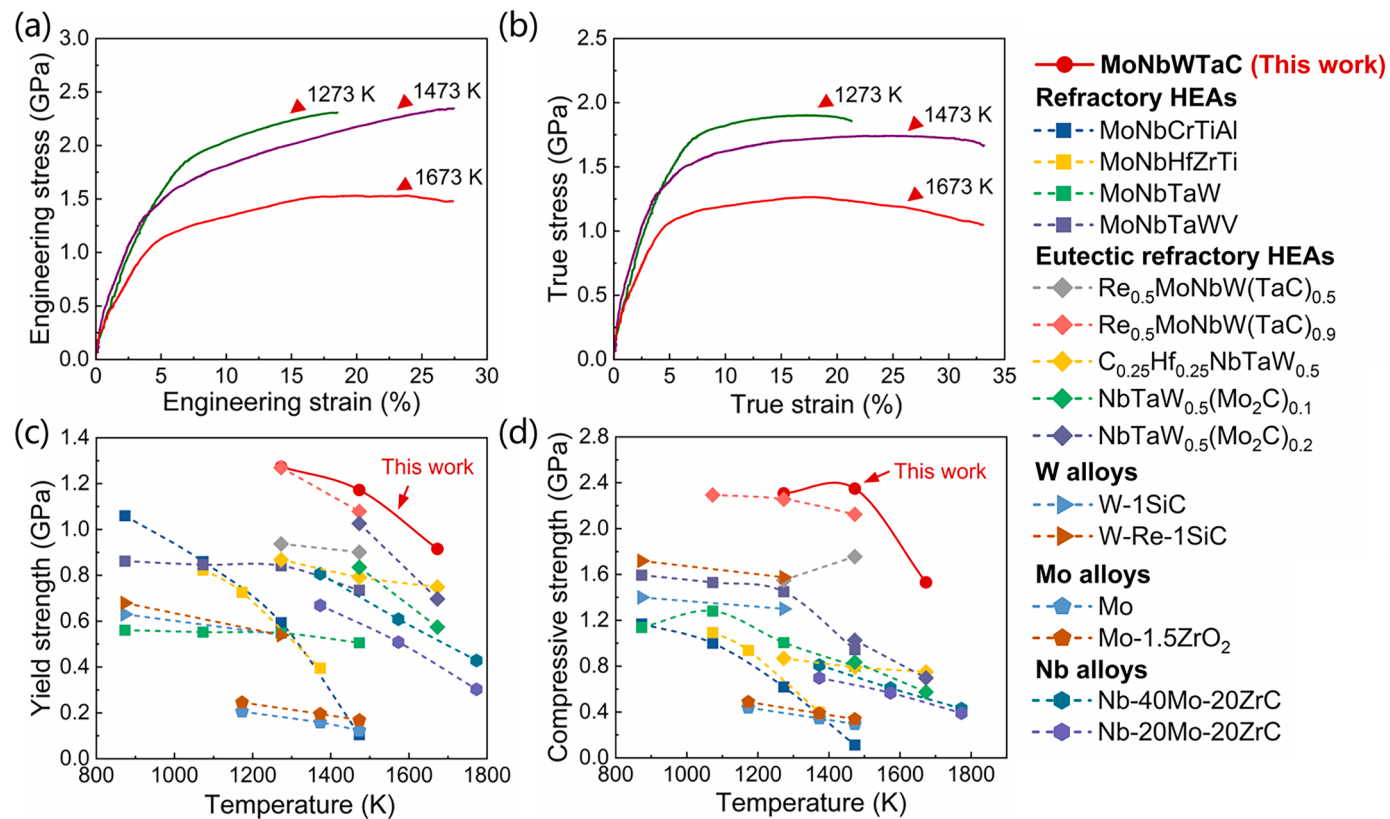
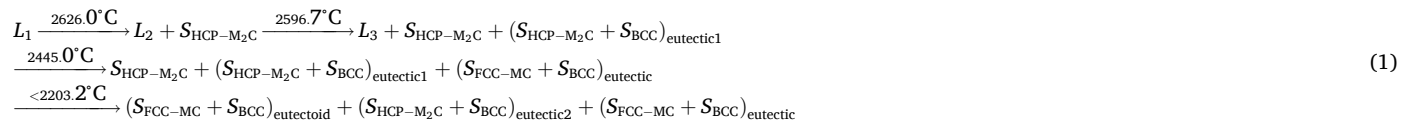


Fig. 2. Compressive properties of the MoNbWTaC HEA. (a-b) Engineering and true stress-strain curves at high temperatures. (c-d) A comparison of the temperature dependence of engineering yield strength and compressive strength for the MoNbWTaC HEA with other reported refractory alloys demonstrates the exceptional high-temperature strength of the MoNbWTaC HEA.

particle size of 2–5 μm were mixed, cold pressed, and melted to synthesize the MoNbWTaC HEA with a molar ratio of 1: 1: 1: 1. The melting process was carried out in an arc melting furnace (ACM-S01) equipped with non-consumable tungsten electrodes under an argon atmosphere. The melting temperature exceeded the melting point of all raw materials (>3900 °C), ensuring that all raw materials were completely melted and fully reacted. The resulting ingots were approximately 25 mm in diameter and 10 mm high. Phase diagrams were calculated using Thermo-Calc software and the SSUB6 database to elucidate the phase formation process. Cylindrical specimens of Φ4 mm × 6 mm were cut, polished, and subjected to compression tests at 1273 K, 1473 K, and 1673 K with a strain rate of $1 \times 10^{-3} \text{ s}^{-1}$ on a Gleeble-3500 thermal simulator, stopping at a true strain of 40% or upon fracture. Crystal structure analysis was conducted using XRD (Bruker D8) with Cu-Kα radiation, and microstructural characterization involved FE-SEM

are similar to the W, TaC, and Nb₂C phases, respectively, with overall shift in peak positions (Fig. 1a), and then they are denoted as BCC, FCC-MC, and HCP-M₂C phases. Quantitative chemical analysis from EPMA shows that the BCC phase is a HEA with a composition of W₄₆Mo₂₉Ta₁₉Nb₆, while the FCC-MC and HCP-M₂C phases are two carbide phases with compositions of Ta₂₄Nb₁₃W₁₁Mo₅C₄₇ and Nb₂C—Nb₃₁Ta₂₃Mo₆W₆C₃₄, respectively (Fig. S1). These three phases were alternately distributed, forming three typical structures: an ultrafine layered structure with layer thickness of approximately 100 nm, a coarse layered structure with a layer thickness of 1–5 μm, and another coarse layered structure with darker contrast in the carbides (Fig. 1b). Phase diagram calculation was conducted to clarify the microstructure formation and demonstrate the rapid solidification process as described below (Fig. S2):



(Quanta FEG250), EBSD (Oxford Symmetry), and TEM (Talos F200S). Chemical composition was analyzed with EPMA (JXA-8530F Plus), and EBSD data were post-processed using Channel 5 software.

Fig. 1(a and b) presents the XRD patterns and SEM-BSE images of the as-cast MoNbWTaC HEA. The alloy consists of a BCC-structured phase (lattice constant: $a = 0.3198 \text{ nm}$), FCC-structured phase ($a = 0.4388 \text{ nm}$), and HCP-structured phase ($a = 0.3084 \text{ nm}$, $c = 0.4870 \text{ nm}$), which

Noted that eutectoid structure is a solid-state reaction characterized by relatively slow atomic diffusion and ultrafine layer thickness. Therefore, the ultrafine layered structure, brighter and darker coarse layered structures are identified as BCC/FCC-MC eutectoid structure, BCC/FCC-MC and BCC/HCP-M₂C eutectic structures, respectively, with volume fractions of approximately 34.60%, 50.48%, and 14.92% as

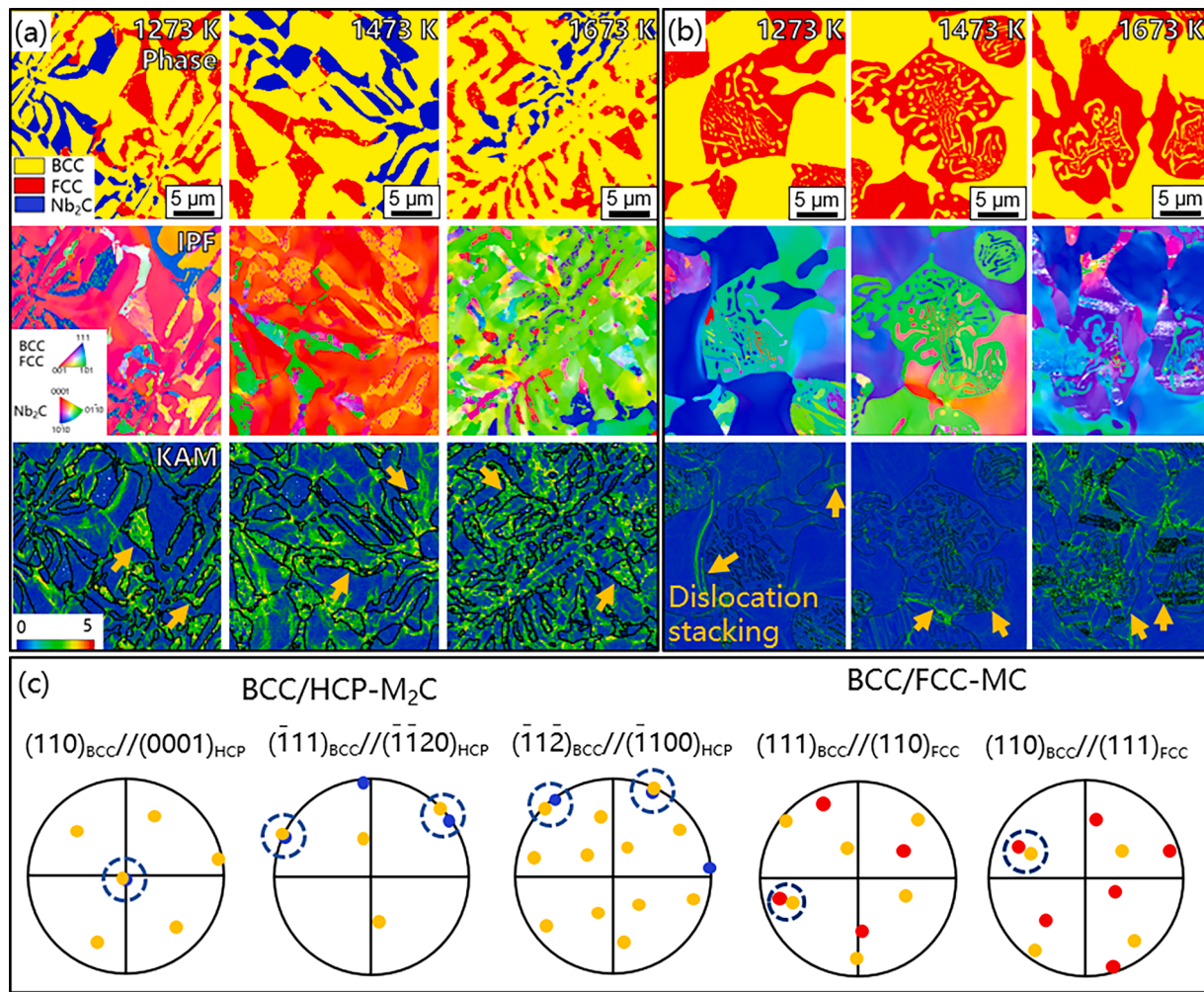


Fig. 3. EBSD maps of the deformed MoNbWTaC HEA. Phase map, IPF, and KAM maps of the (a) eutectic and (b) eutectoid structures. (c) Orientation relationships of the BCC and carbides phases.

measured by Image J software (Fig. 1b).

EBSD analysis was conducted to clarify the phase orientation relationship and dislocation structure. Several eutectic and eutectoid structures were analyzed, and the typical microstructure is shown in Fig. 1(c and d). The BCC and FCC-MC phases in the BCC/FCC-MC eutectic structure and BCC/FCC-MC eutectoid structure have an approximate Kurdjumov-Sachs (K-S) orientation relationship, namely, (111)_{BCC} // (110)_{FCC-MC} and [110]_{BCC} // [111]_{FCC-MC} (Fig. 1e). This indicates similar structural features between the BCC/FCC-MC eutectic structure and BCC/FCC-MC eutectoid structure except for a different layer spacing. The BCC and HCP-M₂C phases have a Burgers orientation relationship of {011}_{BCC} // {0001}_{HCP-M2C}, <111>_{BCC} // <111>_{HCP-M2C}, and <112>_{BCC} // <110>_{HCP-M2C} (Fig. 1e). Dislocation structures in the as-cast HEA were also carefully detected, as presented in the kernel average misorientation (KAM) images. A low dislocation density of 0.18° was detected in the BCC phase, while higher densities of 0.477° and 0.288° were detected in the FCC-MC and HCP-M₂C carbide phases, respectively.

The microstructure of the BCC/FCC-MC eutectoid structure was further measured by TEM [Fig. 1(f-h)]. The BCC phase contains more Mo and W, while the FCC-MC carbide contains more Ta, Nb, and C, consistent with EPMA results (Fig. S1). The TEM image reveals a high dislocation density of stacking faults in the FCC-MC carbide, with intersecting stacking faults at 60° (Fig. 1g), verifying a higher dislocation density in FCC-MC than in the BCC phase [Fig. 1(c and d)]. Specially, the high density of stacking faults in the FCC-MC phase might

be attributable to the Mo and W solutions which could decrease the stacking fault energy of NbC to form numerous stacking faults in the as-cast NbC phase, as reported in our previous work [33]. The BCC and FCC-MC phases have a serrated interface with a well-combined K-S orientation relationship (Fig. 1h). Through calculation based on the Bramfitt lattice matching theory [29,34], the mismatch parameter δ_1 between the (101)_{BCC} plane (with $d = 0.1818 \text{ nm}$) and the (020)_{FCC-MC} plane (with $d = 0.1717 \text{ nm}$) is calculated to be $\delta_1 = \frac{|0.1818 - 0.1717/\cos(2.8)|}{0.1717/\cos(2.8)} \approx 0.06$, while the mismatch parameters δ_2 between (110)_{BCC} and (111)_{FCC-MC} along with δ_3 between (011)_{BCC} and (111)_{FCC-MC} are calculated to be 0.06 and 0.21, respectively. Therefore, the average mismatch parameter δ , considering δ_1 , δ_2 , and δ_3 , is determined to be 11.1% (within the range of 5% to 25%), indicating a semi-coherent interface between the BCC and FCC-MC phases. Theoretically, this in-situ zig-zag semi-coherent interface is formed to adjust for lattice content differences, which has been demonstrated to possess low interfacial energy and high thermal stability.

Fig. 2(a and b) shows the representative high-temperature compressive properties of the as-cast MoNbWTaC HEA. The engineering yield strength at 1273 K is 1.27 GPa, which decreases to 1.17 GPa at 1473 K and 0.92 GPa at 1673 K. The corresponding true yield strength is 1.16 GPa at 1273 K, 0.95 GPa at 1473 K, and 0.89 GPa at 1673 K. Although the strength decreases with increasing temperature, all stress-strain curves exhibit hardening before yielding without obvious softening up to 1673 K. These results demonstrate that the MoNbWTaC HEA

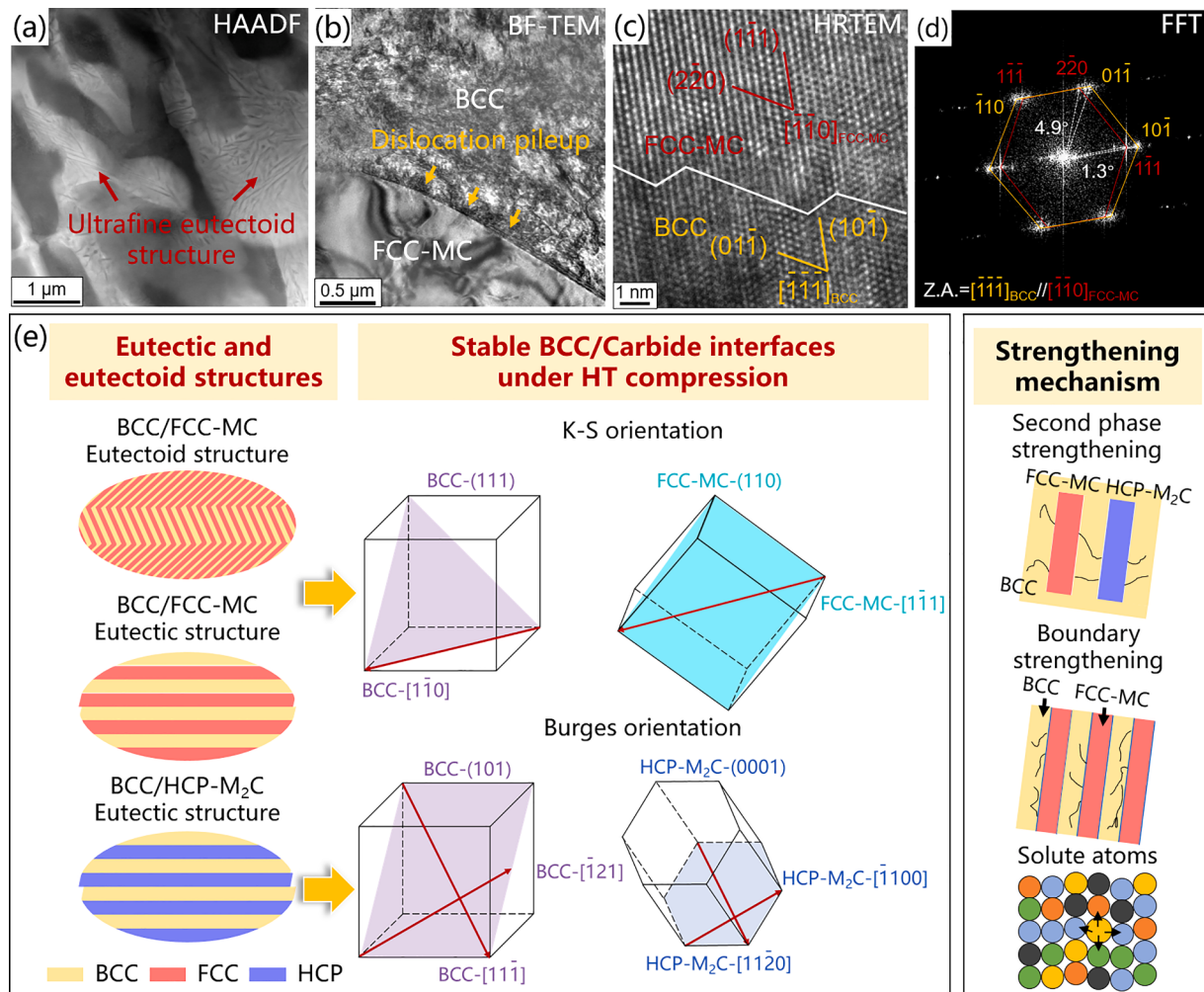


Fig. 4. TEM images of the 1673 K-deformed MoNbWTaC HEA. (a-b) HAADF-STEM and Bright-field TEM images. (c-d) High-resolution TEM and FFT images show a stable interface. (e) Strengthening mechanism diagram.

exhibits exceptional high-temperature strength at temperatures from 1273 K to 1673 K, indicating an excellent reinforcement effect of the eutectic and eutectoid structures. Meanwhile, the MoNbWTaC HEA exhibits an engineering yield strength of 2.06 GPa, compressive strength of 2.61 GPa, and a plastic strain of 7.23% (corresponding to a true strain of 10.27%) at room temperature [27], demonstrating a certain deformation capacity and good processability.

We summarized the high-temperature engineering yield and compressive strength of the MoNbWTaC HEA and other previously reported refractory alloys listed in Fig. 2(c and d) [30–32,35–42]. Obviously, the MoNbWTaC HEA shows the highest yield and compressive strength at high temperatures. It is particularly pointed out that the reported Re_{0.5}MoNbW(TaC)_{0.9} HEA has high thermal stability and exceptional high-temperature strength due to its high melting point and fully eutectic structure with an interwoven metal-carbide interface. Through in-depth comparative analysis with the Re_{0.5}MoNbW(TaC)_{0.9} HEA, the MoNbWTaC HEA shows higher strength, demonstrating that the ultrafine eutectoid structure serves as an important and effective factor for achieving exceptional high-temperature performance.

EBSD measurements of the post-deformation eutectic and eutectoid structures were carried out to analyze the deformation behavior of the MoNbWTaC HEA at high temperatures (Fig. 3). After compression, the BCC/FCC-MC eutectic structure, BCC/HCP-Nb₂C eutectic structure, and BCC/FCC-MC eutectoid structure remain stable in both microscopic morphology and phase orientation relationship, as shown in the IPF and orientation relationship maps. The BCC and FCC-MC phases in the BCC/

FCC-MC eutectic and eutectoid structures maintain the K-S orientation relationship, while the BCC and HCP-Nb₂C phases in the BCC/HCP-Nb₂C eutectic structure maintain the Burgers orientation relationship, demonstrating high thermal and mechanical stability of the eutectic and eutectoid structures.

The changes in dislocation density in the deformed MoNbWTaC HEA were also observed in the KAM maps shown in Fig. 3. Increasing the deformation temperature results in an increase in the overall dislocation density, indicating no obvious dynamic recovery. It is noted that the BCC and FCC-MC phases in the eutectic and eutectoid structures have similar dislocation deformation behavior and KAM values. The KAM values are summarized and plotted in Fig. S3. The BCC phase exhibits a higher deformation behavior with the KAM values increasing by 118% at 1273 K and 202% at 1673 K, while the FCC-MC and HCP-M₂C carbides show limited deformability with the KAM values increasing by less than 45%, indicating a primary deformation contribution of the BCC phase during compression. Upon careful observation, high density dislocations accumulate at the BCC/FCC-MC and BCC/HCP-Nb₂C phase interfaces, as indicated by yellow arrows in the KAM maps, demonstrating effectively dislocation motion hinderance of the carbide phases during deformation. Interestingly, deformation twins were observed in the FCC-MC carbide in both the eutectic and eutectoid structures, the enlarged images are displayed in Fig. S4. The FCC-MC carbide contains numerous 60° ⟨111⟩ twins at temperatures ranging from 1273 K to 1673 K, suggesting a low stacking fault energy of the FCC-MC phase.

The eutectoid structure of the MoNbWTaC HEA after compression at

1673 K was further examined by TEM (Fig. 4). The ultrafine eutectoid structure retains BCC and FCC-MC phases without new phases or recrystallization (Fig. 4a). High densities of dislocations are observed in the BCC and FCC-MC phases, however, the dislocations are obstructed and stacked at the phase interface (Fig. 4b). The high-resolution TEM image of the BCC/FCC-MC phase interface reveals a well-combined interface with a K-S orientation relationship [Fig. 4(c and d)]. Through calculation, the lattice mismatch parameter δ_1 between the $(01\bar{1})_{\text{BCC}}$ plane ($d = 0.2290 \text{ nm}$) and the $(2\bar{2}0)_{\text{FCC-MC}}$ plane ($d = 0.2381 \text{ nm}$) is determined to be $\delta_1 = \left| \frac{0.2381 - 0.2290 / \cos(4.9)}{0.2290 / \cos(4.9)} \right| \approx 0.04$, the lattice

mismatch parameters δ_2 for $(10\bar{1})_{\text{BCC}}$ and $(1\bar{1}\bar{1})_{\text{FCC-MC}}$ and δ_3 for $(\bar{1}10)_{\text{BCC}}$ and $(1\bar{1}\bar{1})_{\text{FCC-MC}}$ are determined to be 0.14 and 0.05, respectively. Thus, the average mismatch parameter δ is calculated to be 7.5%, retaining a semi-coherent interface between the BCC and FCC-MC phases. This lattice mismatch parameter (7.5%) is lower than that of the as-cast HEA (11.1%), suggesting a decreased interfacial strain energy at high temperatures through lattice relaxation and confirming microstructural thermal and mechanical stability.

Generally, high-temperature deformation is primarily governed by diffusion mechanisms such as grain boundary and interface sliding, dislocation recovery, and recrystallization. However, the MoNbWTaC HEA in the present work exhibits excellent thermal stability and superior high-temperature strength without dynamic recrystallization after compression at high temperatures up to 1673 K. Compared with single-phase refractory traditional alloys and HEAs, the high strength of the MoNbWTaC HEA is mainly attributable to the solid solution strengthening and second-phase strengthening, originating from the lattice distortion from multi-principal elements and interlocking interaction of immiscible metal/carbide interfaces, which jointly hinder the element diffusion within the phases and at the interface [43,44]. Further comparison with $\text{Re}_{0.5}\text{MoNbW}(\text{TaC})_{0.9}$ eutectic HEA [30], the MoNbWTaC HEA exhibits higher strength with numerous ultrafine BCC/FCC-MC eutectoid structure, suggesting significant strengthening effect of the fine eutectoid structure. Eutectoid reaction has been demonstrated to be a thermodynamically driven phase transition process to form a stable eutectoid structure by minimizing interface energy and maximizing low-energy planes [45,46]. The resulting BCC/FCC-MC eutectoid structure has a low-energy semi-coherent interface, which remain stable with the lattice mismatch parameter decreased from 11.1% in the as-cast alloy to 7.5% in 1673 K-deformed alloy, showing high thermal and mechanical stability (Fig. 4e). This stable phase interface enables the carbide phase to bear high loads during high-temperature deformation. Meanwhile, for the eutectic materials with lamellar structures, the yield strength (σ_{ys}) has been demonstrated to correlate with average lamellar spacing (λ) with an equation $\sigma_{ys} = \sigma_0 + k_{sp}f\lambda^{-1/2}$ [47,48]. Here, σ_0 is Peierls-Nabarro stress, k_{sp} is a slope constant, and f is the volume fraction of the second phase. Smaller spacing or denser distribution of the second phases have a stronger enhancement by reducing the characteristic length of slip bands in the matrix and providing more phase interfaces to hinder dislocation movement. Thus, the BCC/FCC-MC stable eutectoid structure with ultrafine lamellar spacing significantly enhances the MoNbWTaC HEA to exhibit a superior high-temperature strength by boundary strengthening (Fig. 4e).

In this study, we developed a MoNbWTaC HEA with superior high-temperature yield strengths of 1.17 GPa at 1473 K and 0.92 GPa at 1673 K. The microstructure consists of BCC/FCC-MC eutectic structure, BCC/HCP-M₂C eutectic structure, and BCC/FCC-MC eutectoid structure. The BCC and carbide phases create low-energy interfaces with a specific orientation relationship, which remain stable at temperatures up to 1673 K and effectively hinder dislocation movement, enhancing the alloy. The BCC/FCC-MC eutectoid structure has an ultrafine layer thickness and numerous interfaces, providing a primary strengthening effect. The strategy for developing ultrafine eutectoid structures offers innovative insights for designing and producing the next generation of

high-performance refractory alloys.

CRediT authorship contribution statement

Xiao Wang: Writing – review & editing, Writing – original draft, Methodology, Investigation, Formal analysis, Data curation, Conceptualization. **Guoqiang Luo:** Validation, Supervision, Resources, Funding acquisition. **Qinjin Wei:** Writing – review & editing, Validation, Supervision, Resources, Funding acquisition. **Yi Sun:** Supervision. **Wei Huang:** Software. **Jian Peng:** Software. **Jian Zhang:** Supervision. **Qiang Shen:** Supervision.

Declaration of competing interest

The authors declare that they have no known competing financial interests or personal relationships that could have appeared to influence the work reported in this paper.

Acknowledgments

This work was supported by the National Key R&D Program of China [no. 2021YFB3802300], the Guangdong Major Project of Basic and Applied Basic Research [2021B0301030001], the National Natural Science Foundation of China [no. 52401163], Natural Science Foundation of Hubei Province [no. 2024AFB733], and the Independent Innovation Projects of the Hubei Longzhong Laboratory [no. 2022ZZ-33].

Supplementary materials

Supplementary material associated with this article can be found, in the online version, at doi:10.1016/j.scriptamat.2024.116393.

References

- [1] F. Courty, M. Kaufman, A. Clarke, Solid-solution strengthening in refractory high entropy alloys, *Acta Mater.* 175 (2019) 66–81.
- [2] Y. Hsiao, C. Tung, S. Lin, J. Yeh, S. Chang, Thermodynamic route for self-forming 1.5 nm V-Nb-Mo-Ta-W high-entropy alloy barrier layer: roles of enthalpy and mixing entropy, *Acta Mater.* 199 (2020) 107–115.
- [3] Y. Hu, A. Sundar, S. Ogata, L. Qi, Screening of generalized stacking fault energies, surface energies and intrinsic ductile potency of refractory multicomponent alloys, *Acta Mater.* 210 (2021) 116800.
- [4] I. Kim, H. Oh, K. Lee, E. Park, Optimization of conflicting properties via engineering compositional complexity in refractory high entropy alloys, *Scripta Mater.* 199 (2021) 113839.
- [5] X. Li, W. Li, D. Irving, L. Varga, L. Vitos, Stephan, Ductile and brittle crack-tip response in equimolar refractory high-entropy alloys, *Acta Mater.* 189 (2020) 174–187.
- [6] Q. Liu, G. Wang, X. Sui, Y. Xu, Y. Liu, J. Yang, Ultra-fine grain $\text{Ti}_x\text{VNbMoTa}$ refractory high-entropy alloys with superior mechanical properties fabricated by powder metallurgy, *J. Alloy. Compd.* 865 (2021) 158592.
- [7] F. Maresca, W.A. Curtin, Mechanistic origin of high strength in refractory BCC high entropy alloys up to 1900K, *Acta Mater.* 182 (2020) 235–249.
- [8] V. Soni, B. Gwalami, T. Alam, S. Dasari, Y. Zheng, O.N. Senkov, D. Miracle, R. Banerjee, Phase inversion in a two-phase, BCC+B2, refractory high entropy alloy, *Acta Mater.* 185 (2020) 89–97.
- [9] M. Wang, Z. Ma, Z. Xu, X. Cheng, Effects of vanadium concentration on mechanical properties of VNbMoTa refractory high-entropy alloys, *Mat. Sci. Eng. A-Struct.* 808 (2021) 140848.
- [10] B. Yin, F. Maresca, W. Curtin, Vanadium is an optimal element for strengthening in both fcc and bcc high-entropy alloys, *Acta Mater.* 188 (2020) 486–491.
- [11] X. Han, G. Wu, D.S. He, X. Hong, Single-element amorphous metals, *Interdiscipl. Mater.* 3 (4) (2024) 480–491.
- [12] J. Luo, Computing grain boundary “phase” diagrams, *Interdiscipl. Mater.* 2 (1) (2023) 137–160.
- [13] K. Tian, C. Wei, Z. Wang, Y. Li, B. Xi, S. Xiong, J. Feng, Stable sodium metal anode enabled by interfacial room-temperature liquid metal engineering for high-performance sodium–sulfur batteries with carbonate-based electrolyte, *Interdiscipl. Mater.* 3 (3) (2024) 425–436.
- [14] A. Mostafaei, R. Ghiasiaria, I.T. Ho, S. Strayer, K.C. Chang, N. Shamsaei, S. Shao, S. Paul, A.C. Yeh, S. Tin, A.C. To, Additive manufacturing of nickel-based superalloys: a state-of-the-art review on process-structure-defect-property relationship, *Prog. Mater. Sci.* 136 (2023) 101108.
- [15] O.N. Senkov, G.B. Wilks, D.B. Miracle, C.P. Chuang, P.K. Liaw, Refractory high-entropy alloys, *Intermetallics* 18 (9) (2010) 1758–1765.

- [16] J.W. Yeh, S.K. Chen, S.J. Lin, J.Y. Gan, T.S. Chin, T.T. Shun, C.H. Tsau, S.Y. Chang, Nanostructured high-entropy alloys with multiple principal elements: novel alloy design concepts and outcomes, *Adv. Eng. Mater.* 6 (5) (2004) 299–303.
- [17] Z. Han, N. Chen, S. Zhao, L. Fan, G. Yang, Y. Shao, K. Yao, Effect of Ti additions on mechanical properties of NbMoTaW and VNbMoTaW refractory high entropy alloys, *Intermetallics* 84 (2017) 153–157.
- [18] O.N. Senkov, J.M. Scott, S.V. Senkova, F. Meisenkothen, D.B. Miracle, C. F. Woodward, Microstructure and elevated temperature properties of a refractory TaNbHfZrTi alloy, *J. Mater. Sci.* 47 (9) (2012) 4062–4074.
- [19] O.N. Senkov, G.B. Wilks, J.M. Scott, D.B. Miracle, Mechanical properties of Nb₂₅Mo₂₅Ta₂₅W₂₅ and V₂₀Nb₂₀Mo₂₀Ta₂₀W₂₀ refractory high entropy alloys, *Intermetallics* 19 (5) (2011) 698–706.
- [20] M. Todai, T. Nagase, T. Hori, A. Matsugaki, A. Sekita, T. Nakano, Novel TiNbTaZrMo high-entropy alloys for metallic biomaterials, *Scripta Mater.* 129 (2017) 65–68.
- [21] B. Zhang, M. Gao, Y. Zhang, S. Yang, S. Guo, Senary refractory high entropy alloy MoNbTaTiVW, *Mater. Sci. Tech.-Lond.* 31 (10) (2015) 1207–1213.
- [22] T. Bhattacharjee, R. Zheng, Y. Chong, S. Sheikh, S. Guo, I. Clark, T. Okawa, I. Wani, P. Bhattacharjee, A. Shibata, N. Tsuji, Effect of low temperature on tensile properties of AlCoCrFeNi_{2.1} eutectic high entropy alloy, *Mater. Chem. Phys.* 210 (2018) 207–212.
- [23] X. Gao, Y. Lu, B. Zhang, N. Liang, G. Wu, G. Sha, J. Liu, Y. Zhao, Microstructural origins of high strength and high ductility in an AlCoCrFeNi_{2.1} eutectic high-entropy alloy, *Acta Mater.* 141 (2017) 59–66.
- [24] F. He, Z. Wang, P. Cheng, Q. Wang, J. Li, Y. Dang, J. Wang, C. Liu, Designing eutectic high entropy alloys of CoCrFeNiNb_x, *J. Alloy. Compd.* 656 (2016) 284–289.
- [25] X. Jin, Y. Zhou, L. Zhang, X. Du, B. Li, A novel Fe₂₀Co₂₀Ni₄₁Al₁₉ eutectic high entropy alloy with excellent tensile properties, *Mate Lett.* 216 (2018) 144–146.
- [26] G. Luo, S. Jiang, K. Kang, X. Wang, J. Zhang, Y. Sun, Q. Shen, Eutectic-like composite of MoNbWTaC with outstanding strength and plasticity at elevated temperature, *Mate Lett.* 304 (2021) 130739.
- [27] G. Luo, S. Jiang, Q. Wei, K. Kang, Y. Qian, J. Zhang, Y. Sun, Q. Shen, Microstructure and mechanical properties of MoNbW(TaC)_x composites, *Int. J. Refract. Met. H* 99 (2021) 105574.
- [28] I. Wani, T. Bhattacharjee, S. Sheikh, Y. Lu, S. Chatterjee, P. Bhattacharjee, S. Guo, N. Tsuji, Ultrafine-grained AlCoCrFeNi_{2.1} eutectic high-entropy alloy, *Mater. Res. Lett.* 4 (3) (2016) 174–179.
- [29] Q. Wei, X. Xu, G. Li, G. Luo, J. Zhang, Q. Shen, C. Wu, A carbide-reinforced Re_{0.5}MoNbW(TaC)_{0.8} eutectic high-entropy composite with outstanding compressive properties, *Scripta Mater.* 200 (2021) 113909.
- [30] S. Wu, D. Qiao, H. Zhang, J. Miao, H. Zhao, J. Wang, Y. Lu, T. Wang, T. Li, Microstructure and mechanical properties of CHf_{0.25}NbTaW_{0.5} refractory high-entropy alloys at room and high temperatures, *J. Mater. Sci. Technol.* 97 (2022) 229–238.
- [31] S. Wu, D. Qiao, H. Zhao, J. Wang, Y. Lu, A novel NbTaW_{0.5}(Mo₂C)_x refractory high-entropy alloy with excellent mechanical properties, *J. Alloy. Compd.* 889 (2021) 161800.
- [32] Q. Wei, Q. Shen, J. Zhang, Y. Zhang, G. Luo, L. Zhang, Microstructure evolution, mechanical properties and strengthening mechanism of refractory high-entropy alloy matrix composites with addition of TaC, *J. Alloy. Compd.* 777 (2019) 1168–1175.
- [33] Q. Wei, X. Xu, Q. Shen, G. Luo, J. Zhang, J. Li, Q. Fang, C. Liu, M. Chen, T. Nieh, J. Chen, Metal-carbide eutectics with multiprincipal elements make superrefractory alloys, *Sci. Adv.* 8 (27) (2022) eab02068.
- [34] R. Abbaschian, *Physical Metallurgy Principles - SI Version*, 4th Edition, 2009.
- [35] H. Bei, E. George, Microstructures and mechanical properties of a directionally solidified NiAl-Mo eutectic alloy, *Acta Mater.* 53 (1) (2005) 69–77.
- [36] H. Chen, A. Kauffmann, B. Gorr, D. Schliephake, C. Seemüller, J. Wagner, H. Christ, M. Heilmayer, Microstructure and mechanical properties at elevated temperatures of a new Al-containing refractory high-entropy alloy Nb-Mo-Cr-Ti-Al, *J. Alloy. Compd.* 661 (2016) 206–215.
- [37] C. Cui, Y. Gao, S. Wei, G. Zhang, Y. Zhou, X. Zhu, Microstructure and high temperature deformation behavior of the Mo-ZrO₂ alloys, *J. Alloy. Compd.* 716 (2017) 321–329.
- [38] N. Guo, L. Wang, L. Luo, X. Li, Y. Su, J. Guo, H. Fu, Microstructure and mechanical properties of refractory MoNbHfZrTi high-entropy alloy, *Mater. Des.* 81 (2015) 87–94.
- [39] K. Kang, R. Tu, G. Luo, J. Zhang, J. Zhu, Q. Shen, L. Zhang, Synergetic effect of Re alloying and SiC addition on strength and toughness of tungsten, *J. Alloy. Compd.* 767 (2018) 1064–1071.
- [40] K. Kang, R. Tu, G. Luo, J. Zhang, J. Zhu, Q. Shen, L. Zhang, Mechanical, electrical and thermal properties at elevated temperature of W-Si-C multi-phase composite prepared by arc-melting, *Int. J. Refract. Met. H* 75 (2018) 101–106.
- [41] K. Kang, L. Zhang, G. Luo, J. Zhang, R. Tu, C. Wu, Q. Shen, Microstructural evolution and mechanical behavior of W-Si-C multi-phase composite prepared by arc-melting, *Mat. Sci. Eng. A-Struct.* 712 (2018) 28–36.
- [42] Y. Liu, Y. Zhang, H. Zhang, N.J. Wang, X. Chen, H.W. Zhang, Y.X. Li, Microstructure and mechanical properties of refractory HfMo_{0.5}NbTiV_{0.5}Si_x high-entropy composites, *J. Alloy. Compd.* 694 (2017) 869–876.
- [43] X. Yu, C. Wang, The effect of alloying elements on the dislocation climbing velocity in Ni: a first-principles study, *Acta Mater.* 57 (19) (2009) 5914–5920.
- [44] B. Zhao, P. Huang, L. Zhang, S. Li, Z. Zhang, Q. Yu, Temperature effect on stacking fault energy and deformation mechanisms in titanium and titanium-aluminium alloy, *Sci. Rep.-UK* 10 (1) (2020) 3086.
- [45] J.J. Kramer, Determination of the free energy change of eutectoid reactions, and the interfacial energy in pearlitic eutectoids, 1957.
- [46] S.J. Sun, M. Pugh, Interfacial properties in steel-steel composite materials, *Mat. Sci. Eng. A-Struct.* 318 (1–2) (2001) 320–327.
- [47] I. Baker, F.L. Meng, Lamellar coarsening in Fe₂₈Ni₁₈Mn₃₃Al₂₁ and its influence on room temperature tensile behavior, *Acta Mater.* 95 (2015) 124–131.
- [48] L.Y. Wang, B. Ye, W. Huang, W.J. Ding, Theoretical model of yield strength for eutectic colony microstructure materials, *Scripta Mater.* 231 (2023) 115443.